

Assessment of health indicators to detect the aging state of commercial second-life lithium-ion battery cells through basic electrochemical cycling

Emanuele Micheli^{*}, Patrick Höschel, Syed Muhammad Abbas, Christian Ellersdorfer and Jörg Moser

Vehicle Safety Institute, Graz University of Technology, 8010 Graz, Austria

^{*} Correspondence e.micheli@tugraz.at; Tel.: +43 316 873 30352

Abstract: Upon reaching certain limits, electric vehicle batteries are replaced and may find a second life in various applications. However, the state of such batteries in terms of aging and safety remains uncertain when they enter the second-life market. The aging mechanisms within these batteries involve a combination of processes, impacting their safety and performance. Presently, direct health indicators (HIs) like state of health (SOH) and internal resistance increase are utilized to assess battery aging, but they do not always provide accurate indications of the battery's health state. This study focuses on analyzing various HIs obtained through a basic charging-discharging cycle and assessing their sensitivity to aging. Commercial 50 Ah pouch cells with different aging histories were tested, and the HIs were evaluated. Thirteen HIs out of 31 proved to be highly aging-sensitive, thus good indicators. Namely, SOH upon charging and discharging, Coulombic efficiency, constant current discharge time, voltage relaxation profile trend, voltage-charge area upon discharging, hysteresis open circuit voltage HIs, and temperature difference between the tabs upon charging. The findings offer valuable insights for developing robust qualification algorithms and reliable battery health monitoring systems for second-life batteries, ensuring safe and efficient battery operation in diverse second-life applications.

Keywords: electric vehicles; aged cells; pouch batteries; mobility; safety; reuse; repurpose; circular economy; state of safety; monitoring.

Citation: To be added by editorial staff during production.

Academic Editor: Firstname Last-name

Received: date

Accepted: date

Published: date

Publisher's Note: MDPI stays neutral with regard to jurisdictional claims in published maps and institutional affiliations.



Copyright: © 2023 by the authors. Submitted for possible open access publication under the terms and conditions of the Creative Commons Attribution (CC BY) license (<https://creativecommons.org/licenses/by/4.0/>).

1. Introduction

Lithium-ion batteries are widely used in electric vehicles (EVs), due to their lifetime, performance, and high energy density [1]. The EV's battery is replaced from the vehicle once certain limits are reached, e.g., 80% capacity retention [2,3]. The removed battery can be repurposed for a second-life application [4]. However, accurately determining the aging and safety state of these batteries upon arrival at refurbishing companies remains a challenge. The aging of lithium-ion batteries is a complex phenomenon influenced by a combination of physical and chemical mechanisms typically summarized by the scientific literature in three categories, i.e., loss of active material (LAM), loss of lithium inventory (LLI), and internal resistance increase (IRI) [5–9]. The aging occurring within the cell may pose serious safety risks, e.g., thermal runaway is triggered at lower temperatures [10–12] and the increased plated lithium may more likely lead to an internal short-circuit [13,14]. In addition, the legal framework of second-life batteries is still undefined [15]. Consequently, the development of a standardized procedure to identify the state, especially in terms of safety, of these second-life batteries becomes imperative.

Typically, direct health indicators (HIs), i.e., state of health (SOH) and IRI, are used to assess the battery's aging status [16]. However, these indicators merely provide infor-

mation on the available capacity of the battery but not an accurate indication of the battery's aging or safety state [7]. In fact, a degradation mechanism is not always correlated with the capacity fade of the cell. For example, there may be LAM in the absence of LLI and without capacity fade being observed in the cell [17–19]. Nonetheless, other HIs are sensitive to aging and can give additional information on the battery state.

To address the aforementioned limitations and gain deeper insights into battery aging, this paper introduces a novel comprehensive assessment of HIs derived through a basic charging-discharging cycle, evaluating their sensitivity to aging. The selection of HIs is based on existing literature. Aging affects the electro-thermal behavior of the cell, for example, noticeable changes occur in the voltage-time curve. Aged NMC cells charged in constant current (CC) reach the constant-voltage (CV) phase more rapidly [20,21] and increase the duration of the CV phase [22]. Furthermore, with aging the extracted charge compared to the inserted charge is reduced [23]. This shorter CV phase also affects the current-time curve, resulting in a steeper current decrease in fresh cells [24]. Aging also influences the voltage relaxation profile (VRP) which is extracted during the relaxation time after charging. Aged cells require more time to reach a relaxed voltage, which is lower compared to fresh cells [25,26]. Similarly, the voltage-charge behavior is affected by aging, with aged cells showing a reduced area below the voltage-charge curve [18]. The open circuit voltage (OCV) curve is also impacted by aging, leading to steeper curves and higher voltages [27]. Finally, aged cells generate more heat [28] and display greater thermal heterogeneities across the cell [29]. Thus, considering the input from the literature, the analysis is based on seven curves extracted during the basic charging-discharging cycle. These curves yield a catalog of 31 distinct HIs listed in **Table 1**, the HIs and how they are computed are described in more detail in **Chapter 2**.

Table 1. List of considered HIs.

Reference curve	Health indicator	Description
Voltage-time behavior upon charging [20–22]	State of Health (SOH) upon charging	Ratio of the remaining useful capacity over the nominal capacity
	Constant current charge time (CCCT)	Time needed by the battery to reach the CV phase upon charging
	Constant voltage charge time (CVCT)	Time spent by the battery in the CV phase upon charging
	Ratio CVCT/CCCT	Ratio between CVCT and CCCT
Voltage-time behavior upon discharging [20,21,23]	State of health (SOH) upon discharging	Ratio of the remaining useful capacity over the nominal capacity
	Coulomb efficiency (CE)	Ratio of the charged over the discharged capacity
	Constant current discharge time (CCDT)	Time spent by the battery in the CC phase upon discharging
Current-time behavior during the CV charging phase [24]	Constant voltage current profile (CVCP) – a1	Coefficients a1 of the CVCP profile, see Equation 3
	Constant voltage current profile (CVCP) – a2	Coefficients a2 of the CVCP profile, see Equation 3
	Constant voltage current profile (CVCP) – R2	Coefficient of determination of the CVCP profile, see Equation 3
Voltage-time behavior at the end of charging while waiting [25,26]	Voltage relaxation profile (VRP) – relaxed voltage	Voltage measured after a 2 h waiting time after charging
	Voltage relaxation profile (VRP) – slope	Rate of voltage decrease over time during the last hour of waiting time
Voltage-charge behavior upon cycling	Area VdQ charging	Integral of the voltage over the charge
	Area VdQ discharging	Integral of the voltage over the charge

[18,27,30]	OCV at 15 Ah	Voltage measured at 15 Ah considering the hysteresis OCV curve
	OCV at 25 Ah	Voltage measured at 25 Ah considering the hysteresis OCV curve
	OCV at 35 Ah	Voltage measured at 35 Ah considering the hysteresis OCV curve
	OCV slope between 15-25 Ah	Rate of voltage change over the charge between 15 and 25 Ah in the hysteresis OCV curve
	OCV slope between 25-35 Ah	Rate of voltage change over the charge between 25 and 35 Ah in the hysteresis OCV curve
Thermal evolution upon charging [28]	Peak temperature negative tab	Highest absolute temperature recorded on the negative tab
	Peak temperature positive tab	Highest absolute temperature recorded on the positive tab
	Temperature rise negative tab	Maximum absolute temperature minus the minimum absolute temperature measured on the negative tab
	Temperature rise positive tab	Maximum absolute temperature minus the minimum absolute temperature measured on the positive tab
	Average temperature difference	Average temperature difference between the tabs of the cell
Thermal evolution upon discharging [29]	Maximum temperature difference	Maximum temperature difference between the tabs of the cell
	Peak temperature negative tab	Highest absolute temperature recorded on the negative tab
	Peak temperature positive tab	Highest absolute temperature recorded on the positive tab
	Temperature rise negative tab	Maximum absolute temperature minus the minimum absolute temperature measured on the negative tab
	Temperature rise positive tab	Maximum absolute temperature minus the minimum absolute temperature measured on the positive tab
	Average temperature difference	Average temperature difference between the tabs of the cell
	Maximum temperature difference	Maximum temperature difference between the tabs of the cell

The findings gained from these sensitive HIs hold valuable implications for the development of qualification algorithms, particularly for second-life batteries. Furthermore, the simplicity of the evaluation procedure facilitates its replicability with other cells, enhancing its practicality and potential for widespread application in the field of battery aging research.

2. Materials and Methods

The tested battery cells were commercial 50 Ah pouch cells with nickel-manganese-cobalt oxide cathode (NMC111), graphite anode, and SEPARION® separator [31], intended for use in an EV module. The cell has a nominal voltage of 3.65 V and a specific energy of 147 Wh/kg. For the analysis, cells with different aging histories were tested: F1, F2, A1, and A2, see **Table 2**. Cells F1 and F2 were nearly not electrically cycled while A1 and A2 were electrically cycled inside commercial vehicles. This selection enabled to have two distinct non-electrically aged cells (F1 and F2) as references to be compared with the two differently electrically aged cells (A1 and A2) to see how the different aging affects the investigated HIs.

Table 2. Aging history of tested cells.

Aging history	Calendar aging	Cycling time	Average temperature	Temperature range	Average charging current	Max charging current	Avg dis-charging current	Max dis-charging current
	[years]	[h]	[°C]	[°C]	[A]	[A]	[A]	[A]
F1	7	0	27	10 – 35	38	> 50	19	< –150
F2	10	8	20	–40 – 45	10	> 50	75	< –150
A1	8	1239	21	0 – 40	36	> 50	17	< –150
A2	7	613	27	10 – 35	38	> 50	19	< –150

One cell from each aging history was tested (F1, F2, A1, A2), except for F2 where three cells extracted from different positions in the module were tested (F2_C1, F2_C2, F2_C3), and the test on one of the cells of F2 was repeated 3 times to check the repeatability of the measurement.

The cells were charged with CC-CV (constant-current-constant-voltage) from 0% state of charge (SOC) to 100% SOC with constant-current (CC) of 25 A (C/2) until the upper cut-off voltage of 4.2 V. Once the cut-off voltage is reached, the cells were charged in CV with a cut-off current of 2.5 A (C/20). Then, after 2 hours of waiting time during which the VRP is obtained, the cells were discharged with a CC of 25 A (C/2) until the lower cut-off voltage of 3.0 V. During cycling, the temperature was measured using thermocouples near the tabs, as shown in the sketch in Figure 13.

Voltage-time behavior upon cycling

In the voltage-time curves, the following HIs are measured: SOH upon charging and discharging, Coulombic Efficiency (CE), Constant Current Charge Time (CCCT), Constant Voltage Charge Time (CVCT), CVCT/CCCT, and Constant Current Discharge time (CCDT). The measured HIs are shown in Figure 1.

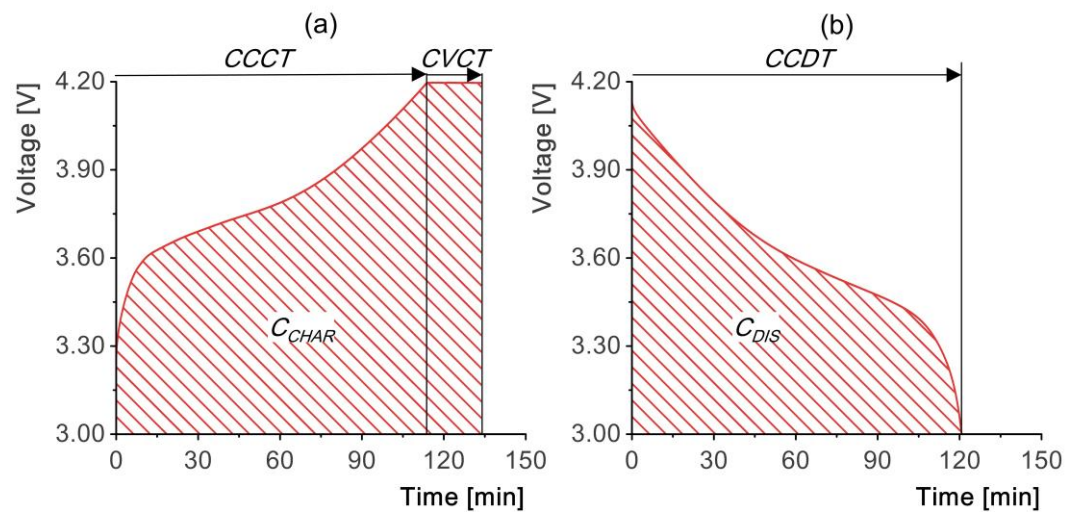


Figure 1. Voltage-time curve upon (a) charging and (b) discharging with extracted HIs.

There are several techniques for estimating SOH, yet due to its simplicity, one of the most widely used methods is coulomb counting [32]. The coulomb counting method is based on the integration of the current I over time t during a full charge or discharge to estimate the inserted or extracted capacity from the battery. The SOH is the ratio of the inserted or extracted charge (depending if it is measured upon charging or discharging) over the rated capacity of the cell C_{RATED} , see Equation 1.

$$SOH = \frac{1}{C_{RATED}} \int Idt \quad (1)$$

CE compares the charge inserted during battery charging C_{CHAR} with the charge extracted during discharging C_{DIS} in order to depict the completeness of the process [23], as shown in **Equation 2**.

$$CE = \frac{C_{CHAR}}{C_{DIS}} \quad (2)$$

The CCCT refers to the time needed to reach the CV phase upon charging. Similarly, CCDT consists in the time taken during discharge to reach the lower cut-off voltage. The CVCT is the time spent during charging in the CV phase, see **Figure 1**.

Current-time behavior during the CV charging phase

From the CV phase upon charging is possible also to extract the Constant Voltage Current Profile (CVCP), shown in **Figure 2**.

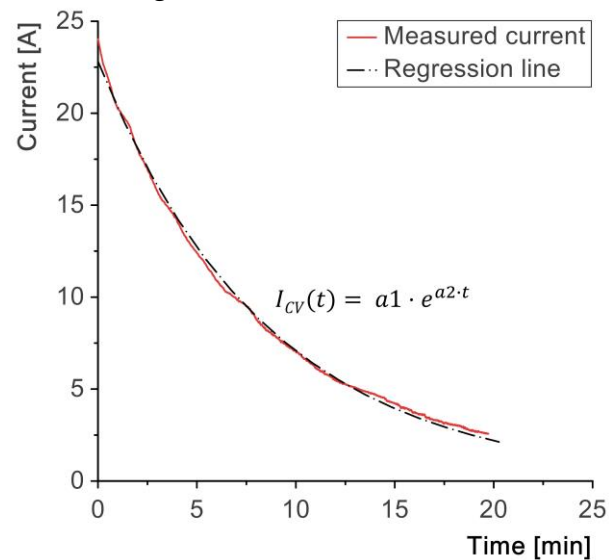


Figure 2. Current-time during CV reference curve. The red line refers to the real data and the black line to the exponential regression function.

During the CV phase, the current decreases following an exponential trend with time. The coefficients $a1$ and $a2$ of the regression function shown in **Equation 3** can be calculated and compared.

$$I_{CV}(t) = a1 \cdot e^{a2 \cdot t} \quad (3)$$

Voltage-time behavior at the end of charging while waiting - Voltage relaxation profile (VRP)

The VRP is the voltage trend during the waiting time at the end of charging, shown in **Figure 3**.

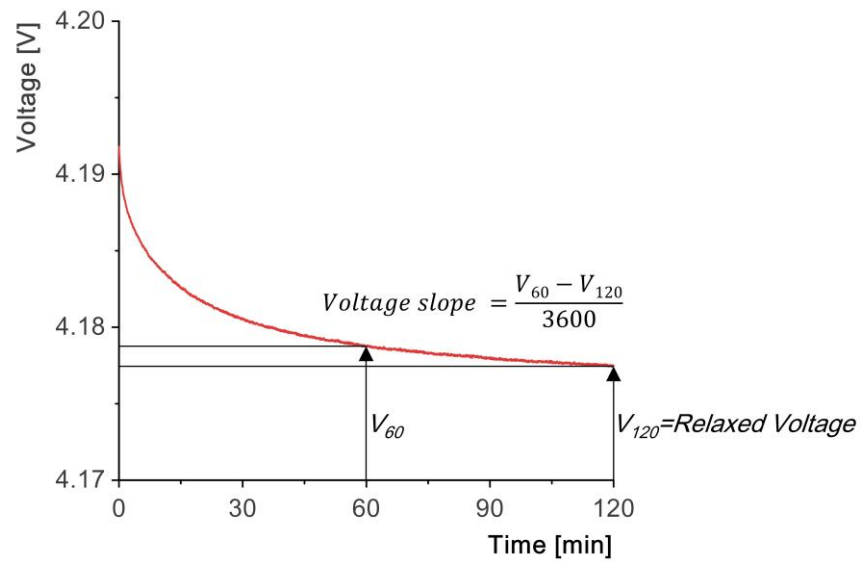


Figure 3. VRP from which the relaxed voltage and the voltage slope HIs are extracted.

The VRP yields two extracted HIs: the relaxed voltage, measured after a two-hour waiting period at the end of charging, and the VRP slope, representing the voltage trend between the first and second hour, calculated with **Equation 4**.

$$\text{Voltage slope} = \frac{V_{60} - V_{120}}{3600} \quad (5)$$

Voltage-charge behavior upon cycling

The voltage-charge curves are shown in **Figure 4**, with the extracted HIs.

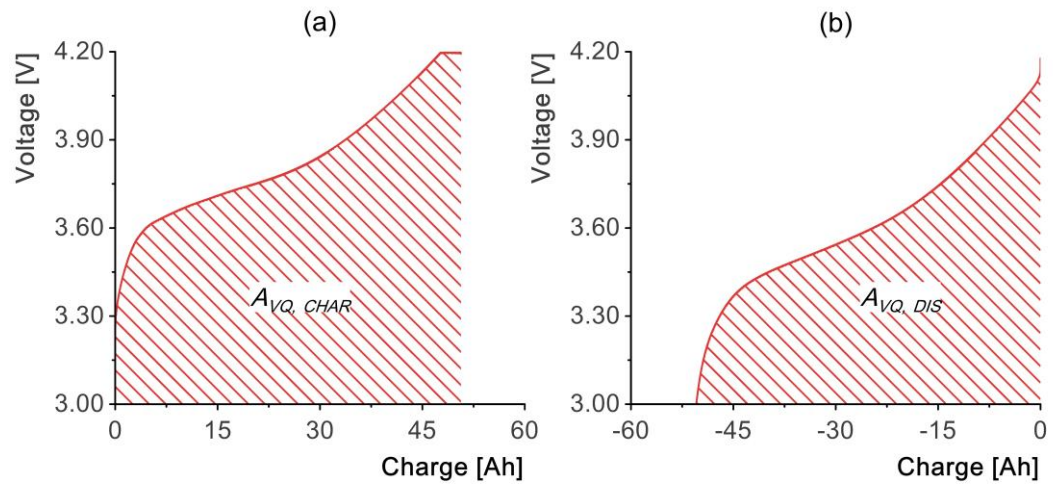


Figure 4. Voltage-charge curves during (a) charging and (b) discharging with the extracted HIs.

The considered HIs refer to the area under the voltage-charge curve A_{VQ} . The area is computed using **Equation 5** with V as voltage and Q as capacity.

$$A_{VQ} = \int V dQ \quad (5)$$

Hysteresis voltage profile – Open circuit voltage (OCV) approximation

Two techniques are commonly used for measuring the OCV curve. The first is "step-wise OCV", which consists of charging up to a certain SOC and then measuring the voltage after a suitable relaxation time [30,33]. The second is "low-current OCV", which consists of charging the battery with a very low current (i.e., < 0.1 C) and considering the battery voltage in a state of quasi-equilibrium. Both of these techniques, however, are time-consuming. An alternative that requires less time is "hysteresis OCV", which consists of averaging the charge and discharge voltage profile over the capacity [34–36] while using higher C-rates and no waiting time. The voltage hysteresis is affected by C-rate, particle size, and electrode thickness [37].

For the OCV approximation, the voltage versus capacity curve during charging is averaged with the curve obtained during discharging (black lines), as shown in **Figure 5**.

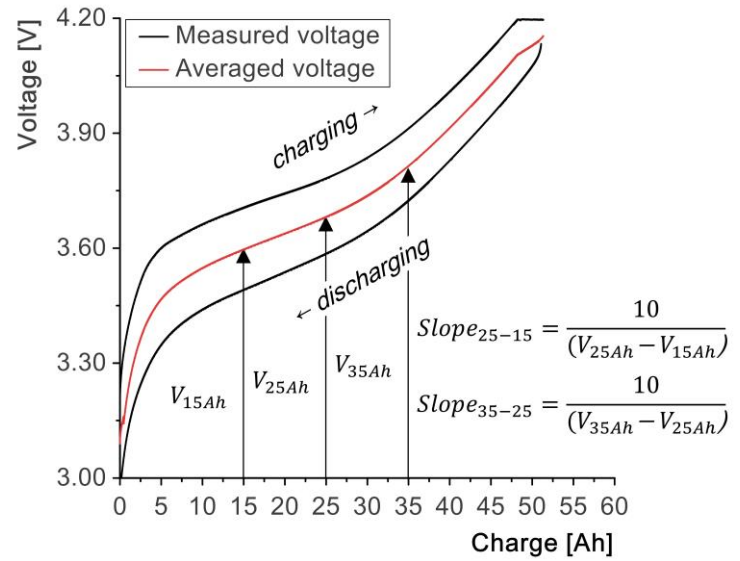


Figure 5. Hysteresis OCV: charging and discharging curve, averaged curve, and HIs extracted.

From the hysteresis OCV curve, five HIs are extracted. Namely the voltage at 15 Ah (30 % SOC), 25 Ah (50% SOC), 25 Ah (70% SOC), the slope (i.e., the change in charge per voltage) between 15 and 25 Ah, and between 25 and 35 Ah. The slope is computed using **Equation 6**.

$$Slope_{x-y} = \frac{\Delta Q_{x-y}}{\Delta V_{x-y}} \quad (6)$$

Thermal evolution upon cycling

The thermal behavior of the cell is also investigated. As shown in **Figure 6** the HIs considered are the maximum absolute temperature reached and the temperature rise, i.e., the maximum minus the minimum temperature measured on either the positive or the negative tab of the cell.

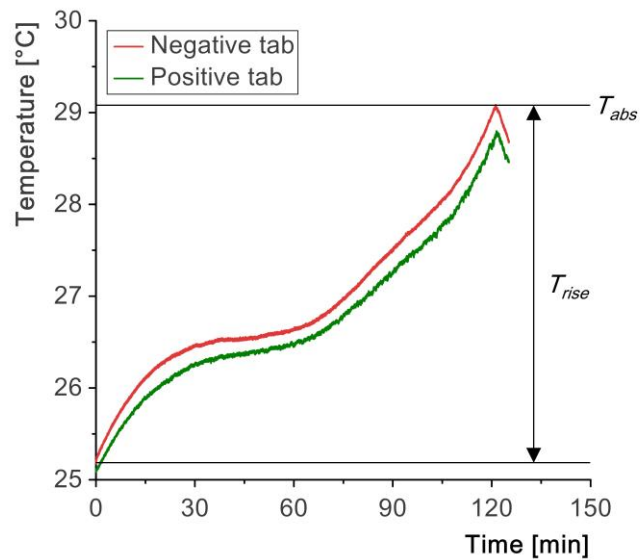


Figure 6. Thermal evolution on the cell. The exemplary thermal rise T_{rise} in this case is referred to the negative tab, a similar procedure is followed for the positive tab.

Additionally, the maximum and the average temperature difference over time between the temperature measured on the positive tab and the negative tab are considered.

Repeatability, sensitivity, and monotonicity assessment

In order to be considered valid HIs, the parameters under investigation must meet certain requirements, namely, independence of starting point, and the possibility of absolute number extraction. It is important to guarantee the independence of starting point since the method is designed for second-life batteries, additionally, the scenario in which no information is available on the state of the battery at the beginning (and during) its first life must be considered. The only information available is the basic information contained in each battery datasheet such as the nominal capacity and the upper and lower voltage limit.

On the other hand, the ability to extract absolute numbers offers a simplified approach to comparing cells by utilizing a single absolute number as a reference. This, in turn, simplifies the implementation of the parameter within algorithms or models.

Furthermore, an evaluation of the HIs is carried out considering repeatability, sensitivity, and monotonicity.

Repeatability refers to the consistency of the HI measurements. A HI with good repeatability will produce consistent results when measured multiple times under the same conditions. Hence, the same HI measured under the same conditions must not spread. *Repeatability* is defined by Equation 6.

$$Repeatability = \frac{\sigma(cycles_{F2_C3})}{\sigma(module_{F2})} \quad (6)$$

With σ referring to standard deviation, the numerator refers to the repetitions conducted on the cell F2_C3 (see Table 2), and the denominator to all the measurements conducted on the cells extracted from F2 (see Table 2). The standard deviation is calculated using Equation 6.

$$\sigma = \frac{\sum(x_i - \bar{x})^2}{N} \quad (6)$$

In the formula x_i refer to each data point, \bar{x} is the dataset average and N is the population size, i.e., the number of measurements included in the dataset.

A lower *Repeatability* value corresponds to a smaller spread of the values obtained by measuring the same cell under the same conditions than the values measured within the

module itself, and thus to a higher score. The application is evaluated for *Repeatability* according to the evaluation scheme shown in **Table 3**.

Sensitivity is a measure of how well a HI can reflect changes in battery aging. The difference between the HI measured for the aged cells and for the non-electrically aged cells must be greater than the spread of the measurements found for the cells extracted from the module containing non-electrically aged cells F2. *Sensitivity* is defined by **Equation 7**.

$$Sensitivity = \frac{\sigma(module_{F2})}{\sigma(dataset)} \quad (7)$$

The denominator refers to the standard deviation of the whole dataset. A lower *Sensitivity* value corresponds to a lower spread of the values obtained by measuring the cells in the same non-electrically aged module compared to the values measured in the whole dataset, indicative of a change of the HI with aging, and thus to a better score. The application is evaluated for repeatability according to the evaluation scheme shown in **Table 3**.

Table 3. Corresponding *Repeatability* and *Sensitivity* scores.

Value	Evaluation scoring
$Repeatability/Sensitivity < 0.25$	4
$0.25 \leq Repeatability/Sensitivity < 0.50$	3
$0.50 \leq Repeatability/Sensitivity < 0.75$	2
$0.75 \leq Repeatability/Sensitivity < 1.00$	1
$Repeatability/Sensitivity > 1.00$	0

Monotonicity refers to a HI's consistent increase or decrease with changes in battery aging. In other words, as batteries age, the measured HI should consistently move in the same direction, either increasing or decreasing, compared to non-electrically aged cells. *Monotonicity* is defined by **Equation 8**.

$$Monotonicity = (F1 - A1)(F1 - A2) \quad (8)$$

F1, A1, and A2 refer to the absolute value of the HI measured on the cell extracted from the corresponding cell ID (see **Table 2**). If the value of *Monotonicity* is less than zero, it implies that the criterion is not met and the HI is not considered appropriate as HI and the score will be zero as shown in **Table 4**.

Table 4. Corresponding *Monotonicity* scores.

Value	Evaluation scoring
$Monotonicity > 0$	1
$Monotonicity < 0$	0

Multiplying the values of *Repeatability*, *Sensitivity*, and *Monotonicity* gives the overall score of the HI under analysis. This makes it possible to rank the HIs under investigation. All HIs with values that are at or above the upper quartile value will be considered good aging-sensitivity HIs, and the remaining poor aging-sensitivity HIs.

3. Results and Discussion

Voltage-time behavior upon cycling

The SOH is measured during both the charging and discharging of the cell using **Equation 1**. The voltage over time charging and discharging curves are shown in **Figure 7**.

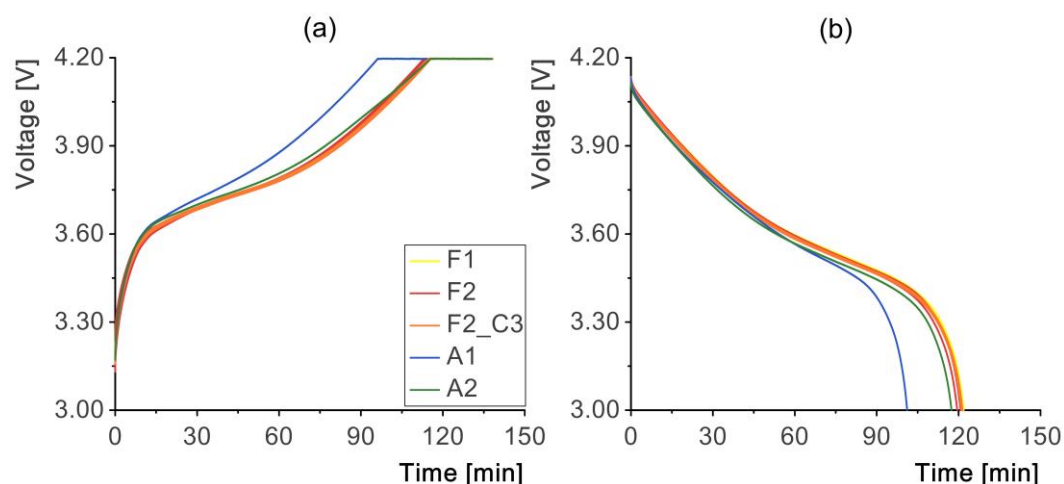


Figure 7. Voltage-time curves during (a) charging and (b) discharging.

The SOH values measured upon charging and discharging follow a similar pattern, the absolute measured values are shown in **Table 5**.

Table 5. Absolute values obtained through the different tests of the HIs: SOH charging, SOH discharging, and Coulombic efficiency.

Cell ID	SOH charging [%]		SOH discharging [%]		Coulombic efficiency [%]	
	Cell	Average	Cell	Average	Cell	Average
F1	99.70	99.70	99.19	99.19	99.48	99.48
F2_C1	98.36		98.27		99.90	
F2_C2	98.17		97.28		99.09	
F2_C3	99.84	99.28	98.54	98.27	98.70	98.99
	99.92		98.48		98.56	
	100.10		98.81		98.71	
A1	81.00	81.00	80.03	80.03	98.80	98.80
A2	97.53	97.53	92.90	92.90	95.26	95.26

The SOH is an indicator of the cell's capacity retention. The capacity of a cell fades with aging mainly due to LAM and LLI [38,39]. F1 and F2 exhibit the highest and very similar capacity retention, in both cases higher than 98%. A2 shows slightly lower capacity retention, while A1 has much lower capacity retention, close to 80%, suggesting a more prominent presence of LAM and LLI within the cell.

The results show that the SOH measured during charging is consistently higher than during discharging for all batteries (F1, F2, A1, and A2). The CE values, listed in **Table 5**, indicate that F1, F2, and A1 have similar average CE values near 99%. In contrast, A2 has a lower CE of almost 95%. Typically, CE is characterized by three phases [23,40–42]. In the first cycles, there is a sharp increase in CE mainly due to the formation and growth of the solid electrolyte interphase (SEI). Afterward, the CE stabilizes around 100% and reaches the stable phase, which is maintained for hundreds of cycles. Finally, the third phase is characterized by a decrease in CE due to a sudden increase in chemical processes within the cell that cause LAM and LLI. The decreasing phase coincides with the capacity “knee” point [43]. Thus, CE is an indicator of the side reactions taking place within the battery [44]. In addition, it can give an indication of capacity fade except when applied in the early

stages, however, this is not a concern when considering second-life batteries that already have an aging history. From the obtained result, it emerges that A2, even if it has higher capacity retention than A1, may be more prone to degradation due to increased chemical side reactions occurring while electrochemically cycling.

The charging and discharging times, used for measuring CCCT, CCDT, CVCT, and the ratio between CVCT and CCCT, are represented in **Figure 7**. The values for the aforementioned HIs are listed in **Table 6**.

Table 6. Absolute values obtained through the different tests of the HIs: CCCT, CVCT, CVCT/CCCT, and CCDT.

Cell ID	CCCT [s]		CVCT [s]		$\frac{CVCT}{CCCT}$ [%]		CCDT [s]	
	Cell	Average	Cell	Average	Cell	Average	Cell	Average
F1	6899	6899	1285	1285	18.63	18.63	7313	7313
F2_C1	6819		1206		17.69		7245	
F2_C2	6775		1292		19.07		7172	
	6870	6850	1391	1324	20.25	19.32	7265	7246
F2_C3	6864		1433		20.87		7262	
	6924		1297		18.74		7286	
A1	5760	5760	1081	1081	18.77	18.77	6071	6071
A2	6920	6920	1363	1363	19.69	19.69	7046	7046

The measured CCCT is similar for F1, F2, and A2 close to 6900 s, while it is lower for A1 with a value of 5760 s. On the other hand, the CCDT is lower for the electrically aged cells (A1, A2) compared to the non-electrically aged cells (F1, F2). The CCCT and CCDT decrease with aging [20,21,45,46], this is due to both IRI which leads to an increase in the polarization of the cell upon charging [44], reaching higher voltages faster, and LAM which contributes to reach faster the cell cut-off voltage [20,21]. From the results obtained, therefore, it can be assumed that A1 and A2 are characterized by higher LAM and IRI.

Similarly to CCCT, CVCT follows a similar trend, with higher values for F1, F2, and A2 compared to A1. The CVCT-based HI indicator bases its idea on the time required increases with aging due to the deceleration of charge transfer caused by the combination of the diffusion time slowdown, porosity changes, and electrolyte conductivity degradation over aging. [22,45,47]. Contrary to what is expected, the CV-phase time is lower for the aged cell A1. This may be related to a higher LLI than LAM for A1 leading to less slowdown in ion intercalation in the active material.

Nonetheless, CVCT is sometimes considered an unreliable HI [21]. An alternative is to consider the percentage of time spent charging in CC compared to the total charging time. The ratio between CCCT and CVCT is lowest for F1 and highest for A2. However, in this case, the results do not appear to be directly related to aging, so no conclusions can be drawn about cell degradation.

Current-time behavior during the CV charging phase

The current trend over time during the CV phase is shown in **Figure 8**.

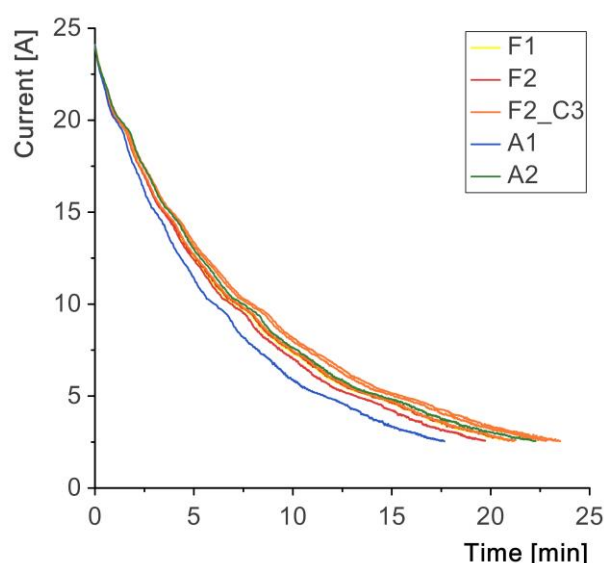


Figure 8. Current-time curve at the end of the CC charging, during the CV phase.

The approximating regression function, which contains coefficients a_1 and a_2 , as well as the coefficient of determination, is based on **Equation 3**, the obtained values are summarised in **Table 7**.

Table 7. Absolute values obtained through the different tests of the CVCP HIs.

Cell ID	a_1		$a_2 \times 10^3$		Coefficient of determination [%]	
	Cell	Average	Cell	Average	Cell	Average
F1	22.49	22.49	-1.83837	-1.84	99.57	99.57
F2_C1	22.81		-1.94976		99.73	
F2_C2	22.49		-1.82381		99.60	
F2_C3	22.49	22.57	-1.68784	-1.78	99.63	99.64
	22.51		-1.64915		99.60	
	22.54		-1.81335		99.63	
A1	22.83	22.83	-2.21677	-2.22	99.69	99.69
A2	22.75	22.75	-1.77636	-1.78	99.60	99.60

The results reveal that the coefficient a_1 of the CVCP is higher for A1 and A2 compared to F1 and F2. On the other hand, the coefficient a_2 is smaller for A1 compared to the other cells. As additional information, the coefficient of determination is higher for A1 compared to F1, F2, and A2.

As mentioned above, aging affects the CV phase [24]. In particular, the time spent during CV-charging increases with aging [22]. Thus by analyzing the CVCP a steeper current decrease (higher coefficient a_1 and lower coefficient a_2) is expected for the non-electrically aged cells (F1, F2). The findings are in line with the CVCT findings, A1 has a higher coefficient a_1 , and a lower coefficient a_2 . This behavior can again be explained by a higher LLI than LAM for cell A1.

Voltage-time behavior at the end of charging while waiting - Voltage relaxation profile (VRP)

The voltage trend over time at the end of the charge is shown in **Figure 9**.

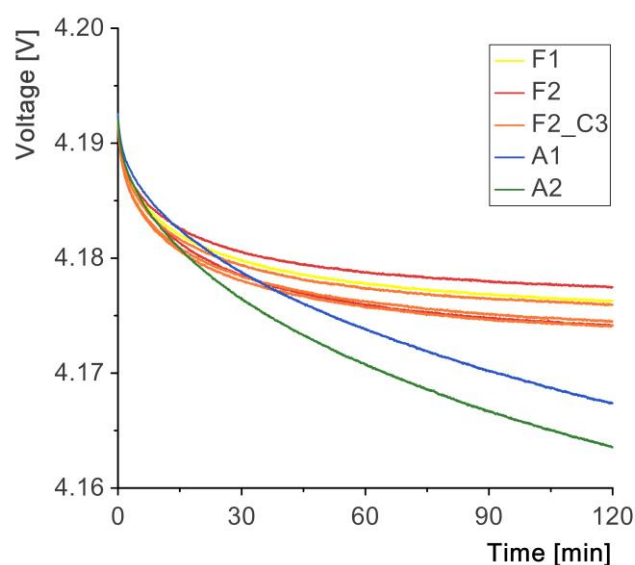


Figure 9. Voltage trends over time (i.e., VRP) at the end of the CC-CV charge.

For each tested cell the voltage measured at the tabs after two hours and the voltage slope with respect to the time between the first and second hour are measured, the obtained values are shown in **Table 8**.

Table 8. Absolute values obtained through the different tests of the VRP HIs.

Cell ID	Relaxed voltage [V]		Voltage trend [$V \times 10^{-6}/s$]	
	Cell	Average	Cell	Average
F1	4.176	4.176	−0.040	−0.040
F2_C1	4.178		−0.032	
F2_C2	4.174		−0.051	
F2_C3	4.175	4.175	−0.042	−0.040
	4.175		−0.039	
	4.176		−0.039	
A1	4.168	4.168	−0.165	−0.165
A2	4.163	4.163	−0.213	−0.213

From the VRP it is shown that aged cells A1 and A2 relaxed to a lower voltage (below 4.17 V) value compared to cells F1 and F2 (above 4.17 V). A difference between A1 and A2 and F1 and F2 emerges also in the VRP slope and, in the last hour, the voltage of A1 and A2 drops faster compared to F1 and F2.

The VRP at the end of charging is correlated with aging. Aged cell' voltage tends to relax to a lower voltage and requires more time to reach an equilibrium point [25,26]. The aging-related change in behavior is related to LLI and LAM, both of which reduce the amount of intercalable ions in the anode. In addition, LAM leads to a change in the crystal structure, which intrinsically affects the voltage measured at the battery electrodes [26,48]. Thus, considering the obtained results, worse behavior in both electrically aged cells A1 and A2 was found. Considering the results, both electrically aged cells A1 and A2 exhibit worse behavior, suggesting the presence of LAM and LLI as a degradation mechanism for both cells.

Voltage-charge behavior upon cycling

The values of the area contained under the Voltage-Capacity curve during charging and discharging are shown in **Figure 10**.

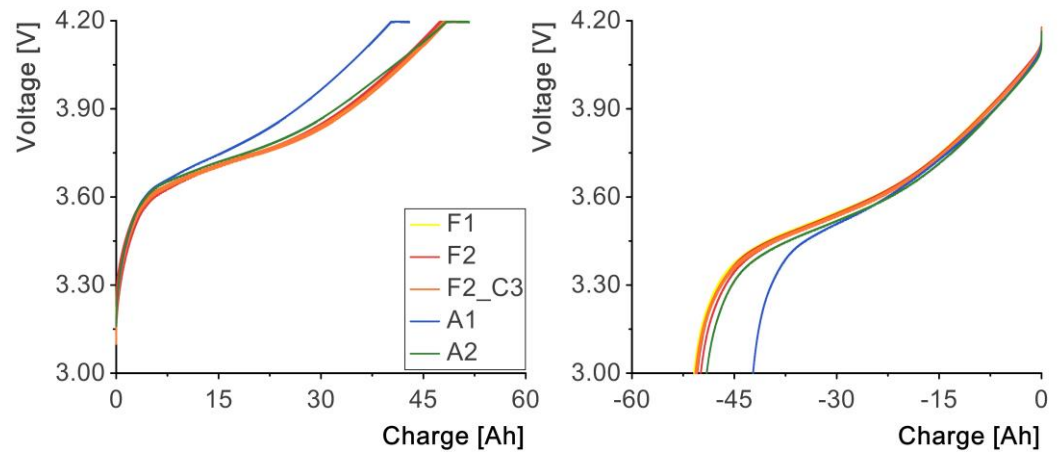


Figure 10. Voltage-charge curves during (a) charging and (b) discharging.

The voltage-capacity curve area values are summarized in **Table 9**.

Table 9. Absolute values obtained through the different tests of the voltage-capacity curve area upon charging and upon discharging.

Cell ID	Voltage-capacity curve area upon charging [VAh]		Voltage-capacity curve area upon discharging [VAh]	
	Cell	Average	Cell	Average
F1	196.47	196.47	185.06	185.06
F2_C1	194.00		183.36	
F2_C2	193.32		181.25	
F2_C3	197.00	195.71	183.39	183.05
	197.11		183.18	
	197.13		184.05	
A1	165.03	165.03	154.44	154.44
A2	198.84	198.84	177.44	177.44

Similarly to the SOH, during aging there is a gradual shrinking of the area under the voltage-capacity curve. The shrinking of the area can be related to various degradation mechanisms and in particular to LLI and LAM [18]. While during charging there is a lower value for A1 but similar values for F1, F2, and A2. During discharging, the values of A1 and A2 are lower than the values calculated for F1 and F2, suggesting LLI and LAM for the electrically aged cells.

Hysteresis voltage profile – Open circuit voltage (OCV) approximation

The hysteresis OCV curves for all cells tested are shown in **Figure 11**.

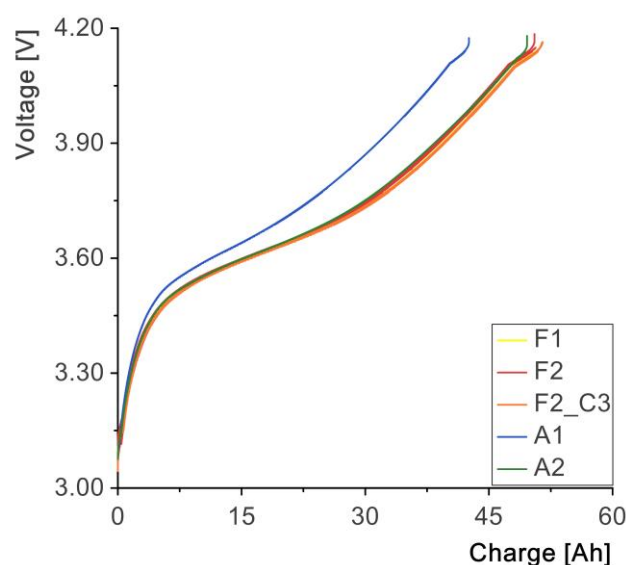


Figure 11. Hysteresis voltage profile results.

The voltage values at 15 Ah, 25 Ah, and 35 Ah, as well as the slopes between 15 Ah and 25 Ah, and between 25 Ah and 35 Ah are considered as HIs, the measured values are shown in **Table 10**.

Table 10. Absolute values obtained through the different tests of hysteresis OCV curve HIs.

Cell ID	Voltage (35 Ah)		Voltage (25 Ah)		Voltage (15 Ah)		Voltage change (35-25 Ah)		Voltage change (25-15 Ah)	
	[V]		[V]		[V]		[Ah/V]		[Ah/V]	
	Cell	Average	Cell	Average	Cell	Average	Cell	Average	Cell	Average
F1	3.81	3.81	3.68	3.68	3.60	3.60	75.29	75.29	117.73	117.73
F2_C1	3.82		3.68		3.60		72.44		115.67	
F2_C2	3.83		3.69		3.59		70.25		109.74	
F2_C3	3.81	3.82	3.68	3.68	3.59	3.59	74.77	73.36	116.69	115.05
	3.81		3.68		3.59		74.40		115.95	
	3.81		3.68		3.59		74.93		117.19	
A1	3.98	3.98	3.78	3.78	3.64	3.64	50.37	50.37	72.54	72.54
A2	3.83	3.83	3.69	3.69	3.60	3.60	68.62	68.62	110.05	110.05

Generally, both at 35 Ah and 25 Ah and 15 Ah, cells A1 and A2 exhibit higher voltages than F1 and F2 for the same capacity. Additionally, both capacity-voltage slopes between the considered capacities are lower for A1 and A2 cells compared to F1 and F2.

For all the five HIs extracted from the hysteresis OCV curve, a worse behavior for the electrically aged cells emerged. In general, the OCV curve is influenced by LAM, LLI, and IRI, thus it cannot be used to detect a specific degradation mechanism and it can be used to detect multiple degradation mechanisms [27] providing an overall idea of the aging state of the battery.

Thermal evolution upon cycling

The graphs in **Figure 12** show the temperature evolution at different positions on the cell (i.e., near the negative tab and the positive tab) during charging and discharging. The absolute maximum temperature and the temperature rise are measured.

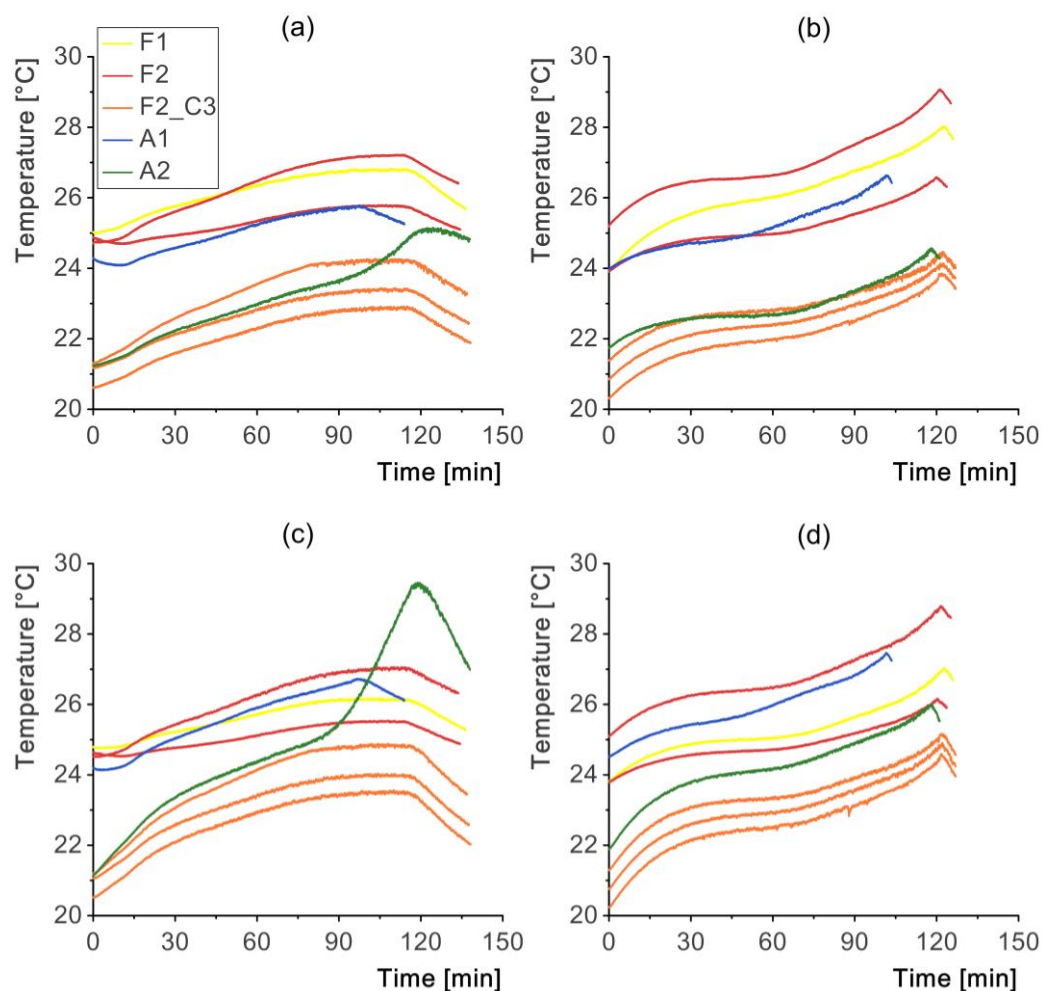


Figure 12 Temperature evolution during charging (a) and discharging (b) measured close to the negative tab and during charging (c) and discharging (d) measured close to the positive tab.

The thermal values measured during charging are shown in **Table 11**.

Table 11. Absolute values obtained through the different tests of the following thermal HIs: maximum absolute temperature on the positive and negative tab upon charging and discharging.

Cell ID	Max T negative tab upon charging [°C]		Max T negative tab upon discharging [°C]		Max T positive tab upon charging [°C]		Max T positive tab upon discharging [°C]	
	Cell	Average	Cell	Average	Cell	Average	Cell	Average
F1	26.83	26.83	28.04	28.04	26.18	26.18	27.04	27.04
F2_C1	27.22		29.09		27.07		28.80	
F2_C2	25.80		26.59		25.54		26.17	
F2_C3	23.44	24.73	24.14	25.63	24.04	25.02	24.91	25.93
	22.92		23.85		23.57		24.60	
	24.27		24.47		24.88		25.17	
A1	25.79	25.79	26.64	26.64	26.73	26.73	27.47	27.47
A2	25.15	25.15	24.57	24.57	29.47	29.47	26.01	26.01

The maximum absolute temperatures on the negative tab ranged from 24.73°C to 26.83°C, with F2 exhibiting the highest temperature and F2 showing the lowest. On the positive tab, the maximum absolute temperatures during charging varied from 25.02°C to 29.47°C, with A2 displaying the highest value. The temperature rise on the negative tab upon charging was found to be in the range of 1.72°C to 3.93°C, with A2 experiencing the most significant temperature rise and F1 showing the smallest increase. On the positive tab, the temperature rise during charging ranged from 1.44°C to 8.32°C, again with A2 showing the highest temperature rise.

The thermal values measured during discharging are shown in **Table 12**.

Table 12. Absolute values obtained through the different tests of the following thermal HIs: absolute temperature rise on the positive and negative tab upon charging and discharging.

Cell ID	T rise negative tab upon charging [°C]		T rise negative tab upon discharging [°C]		T rise positive tab upon charging [°C]		T rise positive tab upon discharging [°C]	
	Cell	Average	Cell	Average	Cell	Average	Cell	Average
F1	1.84	1.84	4.13	4.13	1.44	1.44	3.24	3.24
F2_C1	2.53		3.91		2.56		3.71	
F2_C2	1.12		2.68		1.03		2.39	
F2_C3	2.28	2.25	3.30	3.31	2.98	2.67	4.16	3.70
	2.32		3.55		3.06		4.38	
	2.98		3.10		3.70		3.88	
A1	1.72	1.72	2.67	2.67	2.61	2.61	2.97	2.97
A2	3.93	3.93	2.84	2.84	8.32	8.32	4.13	4.13

The maximum absolute temperatures on the negative tab ranged from 24.57°C to 28.04°C, with F1 having the highest value and A2 having the lowest. On the positive tab, the maximum absolute temperatures during discharging varied from 25.93°C to 27.47°C, with A1 exhibiting the highest temperature. The temperature rise on the negative tab upon discharging was observed to be in the range of 2.67°C to 4.13°C, with F1 experiencing the highest temperature rise. On the positive tab, the temperature rise during discharging ranged from 2.97°C to 4.13°C, with Cell A2 demonstrating the highest temperature rise.

The temperature generated during charging or discharging, due to the ohmic effect, is correlated with the internal resistance of the battery [28,29,49,50]. Due to IRI, aged cells are expected to have a higher temperature rise. In general, cell A2 presented a worse thermal behavior with higher heat generation, this can be related to a greater IRI compared to the other cells.

The evolution of the temperature difference between the positive and negative tab during cell charging and discharging is shown in **Figure 13**.

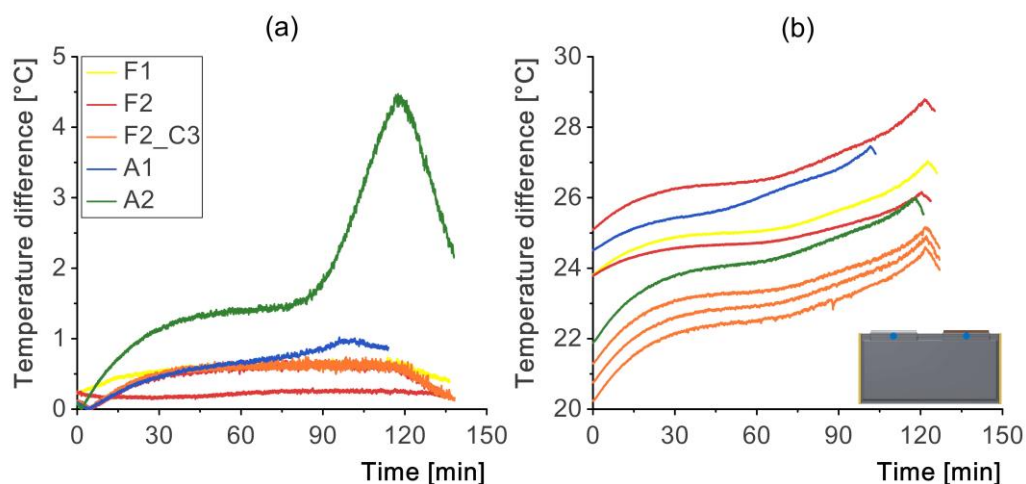


Figure 13 Temperature difference during charging (a) and discharging (b) between the measurement taken close to the negative tab and the positive tab.

The average and maximum temperature difference during charging and discharging are measured and listed in **Table 13**.

Table 13. Absolute values obtained through the different tests of the following thermal HIs: average and maximum temperature difference between tabs upon charging and discharging.

Cell ID	Average T difference upon charging [°C]		Average T difference upon discharging [°C]		Maximum T difference upon charging [°C]		Maximum T difference upon discharging [°C]	
	Cell	Average	Cell	Average	Cell	Average	Cell	Average
F1	0.56	0.56	0.74	0.74	0.87	0.87	1.19	1.19
F2_C1	0.18		0.27		0.21		0.39	
F2_C2	0.22		0.30		0.29		0.49	
F2_C3	0.47	0.37	0.71	0.55	0.51	0.41	0.85	0.68
	0.50		0.74		0.52		0.82	
	0.48		0.74		0.51		0.86	
A1	0.60	0.60	1.02	1.02	0.75	0.75	0.90	0.90
A2	1.87	1.87	4.47	4.47	1.30	1.30	1.62	1.62

In general, higher values are observed on A2 than on F1, F2, and A1. Upon charging, the average temperature differences for the cells ranged from 0.37°C (F2) to 1.87°C (A2), while the maximum temperature differences varied from 0.41°C (F2) to 1.30°C (A2). Similarly, during discharging, the average temperature differences ranged from 0.55°C (F2) to 4.47°C (A2), with the maximum temperature differences ranging from 0.68°C (F2) to 1.62°C (A2). These findings indicate notable variations in the thermal behavior of the cells during charge and discharge cycles, with Cell A2 consistently displaying the most significant temperature differences, both in terms of average and maximum values. This behavior can be because aging leads to heterogeneous cell behavior [51]. At thermal level, this is mainly related to IRI which leads to increased heat generation [28,29,49,50] and to local lithium plating, i.e., LLI, which results in inhomogeneous current densities and thus inhomogeneous temperature distribution upon cycling [52,53].

Repeatability, sensitivity, and monotonicity assessment

Once all absolute HI values have been extracted and/or calculated, *Repeatability*, *Sensitivity*, and *Monotonicity* are calculated. **Table 5** summarizes the values for all the HIs considered in the analysis with the final score in the last column.

Table 5. *Repeatability*, *Sensitivity*, and *Monotonicity* values and final score for the investigated HIs.

Health indicator	<i>Repeatability</i>		<i>Sensitivity</i>		<i>Monotonicity</i>		Final Score
	Value	Score	Value	Score	Value	Score	
SOH charging	0.13	4	0.14	4	4.10E+01	1	16
OCV – 35 Ah	0.22	4	0.13	4	3.20E–03	1	16
OCV – Slope (15–25 Ah)	0.19	4	0.19	4	3.50E+02	1	16
OCV – Slope (25–35 Ah)	0.12	4	0.23	4	1.70E+02	1	16
Max T difference charging	0.07	4	0.17	4	1.10E+00	1	16
SOH discharging	0.27	3	0.09	4	1.20E+02	1	12
Coulombic efficiency	0.14	4	0.37	3	2.90E+00	1	12
CCDT	0.27	3	0.1	4	3.30E+05	1	12
VdQ discharging	0.39	3	0.1	4	2.30E+02	1	12
VRP – V trend	0.27	3	0.09	4	2.20E–02	1	12
OCV – 15 Ah	0.47	3	0.18	4	4.70E–05	1	12
OCV – 25 Ah	0.36	3	0.12	4	6.80E–04	1	12
Average T difference charging	0.1	4	0.28	3	5.70E–02	1	12
VRP – Relaxed V	0.47	3	0.28	3	1.20E–04	1	9
T rise positive tab charging	0.36	3	0.43	3	8.10E+00	1	9
Peak T positive tab charging	0.44	3	0.7	2	1.80E+00	1	6
CVCP – a1	0.16	4	0.85	1	9.00E–02	1	4
CVCP – R2	0.3	3	0.94	1	4.80E–07	1	3
T rise negative tab discharging	0.45	3	0.8	1	1.90E+00	1	3
CCCT	0.53	2	0.14	4	–2.40E+04	0	0
CVCT	0.71	2	0.77	1	–1.60E+04	0	0
CVCT/CCCT	0.8	1	1.19	0	1.60E–01	1	0
CVCP – a2	0.65	2	0.65	2	–2.30E–08	0	0
VdQ charging	0.03	4	0.16	4	–7.40E+01	0	0
Peak T negative tab charging	0.35	3	1.1	0	1.80E+00	1	0
Peak T negative tab discharging	0.13	4	1.08	0	4.80E+00	1	0
Peak T positive tab discharging	0.15	4	1.14	0	–4.50E–01	0	0
T rise negative tab charging	0.52	2	0.77	1	–2.70E–01	0	0
T rise positive tab discharging	0.29	3	1.09	0	–2.30E–01	0	0
Average T difference discharging	0.02	4	0.4	3	–5.20E–02	0	0
Max T difference discharging	0.09	4	0.56	2	–1.20E–01	0	0

Comparing the final score of the 31 HIs shows that some of them score higher than the others given considering *Repeatability*, *Sensitivity*, and *Monotonicity* scores. This allows a ranking to be made. All HIs that scored 12 or higher (upper-quartile) are considered to have good aging-sensitivity. All HIs between one and nine are considered to have lower aging-sensitivity and thus have less weight in the analysis.

Finally, HIs with zero scores are not considered robust HIs and therefore are not considered in the analysis.

Additionally, the monotonicity criterion applied in this study played a crucial role in assessing the changes in HI values for aged cells compared to the non-electrically aged cells. The criterion ensured that the HIs exhibited consistent behavior in the same direction as the cells aged. Interestingly, when the monotonicity criterion was met, two distinct scenarios emerged: A1 exhibited worse behavior than A2 in some cases, while in other instances, the opposite trend was observed, with A2 showing more significant degradation than A1. These contrasting outcomes underscore the influence of different aging histories on the degradation mechanisms experienced by individual cells. It highlights that different degradation processes can be involved, depending on the unique aging conditions experienced by each cell. As a result, the identification of highly sensitive HIs that meet the monotonicity criterion offers a valuable tool to discern and spot the diverse degradation mechanisms that can occur in lithium-ion batteries during their operational lifetime.

Table 6 summarizes the HIs considered and their associated degradation mechanisms and the respective cell with the most critical score.

Table 6. Aging-sensitive HI list with corresponding degradation mechanism and the electrically aged cell where it has shown worse behavior.

Health indicator	Main degradation mechanism	Electrically aged cell
SOH charging	LAM, LLI	A1
OCV – 35 Ah	LAM, LLI	A1
OCV – Slope (15-25 Ah)	LAM, LLI, IRI	A1
OCV – Slope (25-35 Ah)	LAM, LLI, IRI	A1
Max T difference charging	LLI, IRI	A2
SOH discharging	LAM, IRI	A1
Coulombic efficiency	LAM, LLI	A2
CCDT	LAM, LLI	A1
VdQ discharging	LAM, LLI	A1
VRP – V trend	LAM	A2
OCV – 15 Ah	LAM, LLI, IRI	A1
OCV – 25 Ah	LAM, LLI, IRI	A1
Average T difference charging	LLI, IRI	A2
VRP – Relaxed V	LAM	A2
T rise positive tab charging	IRI	A1
Peak T positive tab charging	IRI	A1
CVCP – a1	LLI	A1
CVCP – R2	-	A1
T rise negative tab discharging	IRI	A2

In summary, based on the experimental data of the HIs with scores greater than zero and on the monotonicity study, it can be concluded that cell A1 exhibits a predominant degradation mechanism of LLI, followed by LAM. On the other hand, for cell A2, the primary degradation mechanism is LAM, with IRI also playing a significant role.

This investigation's limitations stem from the limited number of cells tested and the restriction to a single type per chemistry and shape.

5. Conclusions

Several HI found in the scientific literature were evaluated through a series of tests performed on 50 Ah commercial pouch cells. The aim was to obtain the most suitable HIs for qualifying second-life batteries considering their aging-sensitivity. The aging-sensitivity assessment was performed considering three criteria: repeatability, sensitivity, and monotonicity. The tests were conducted on four cells with different aging histories (F1, F2, A1, A2). In particular, two (A1 and A2) were electrically aged. The study showed that of the 31 HI:

- 13 have good aging-sensitivity (i.e., SOH measured upon charging and discharging, the CE, the CCDT, the voltage trend extracted from the VRP, VdQ measured upon discharging, all the values extracted from the OCV curve, the maximum and average temperature difference between the tabs measured upon charging);
- 6 have poor aging-sensitivity (i.e., temperature rise measured on the positive tab upon charging, the relaxed voltage at the end of the VRP, the absolute peak temperature measured on the positive tab upon charging, α_1 coefficient from the CVCP, R_2 coefficient from the CVCP, and the temperature rise measured on the negative tab upon discharging);
- 12 failed to meet one of the criteria for sensitivity, repeatability, or monotonicity and thus are not suitable for battery qualification.

From the obtained results it emerged that the behavior of some HIs differed when comparing the electrically aged cells, indicating that different aging histories can affect degradation phenomena differently within the cell. Specifically, cell A1 displayed a predominant degradation mechanism of LLI, followed by LAM, while A2 predominantly showed IRI and LAM. This highlights the need to consider multiple HIs for battery qualification, as different aging conditions may impact degradation differently.

The implications of these findings are significant for battery health monitoring systems, ensuring safe and efficient battery operation across various applications. By identifying and monitoring these sensitive HIs, more accurate assessments of battery aging and health can be achieved, enabling proactive maintenance and safety measures. Furthermore, the knowledge gained from this study is valuable for the evaluation of second-life batteries, assisting in the determination of their suitability for reuse and repurposing.

However, it is important to acknowledge that the study focused on aging-sensitivity, and the next step involves narrowing down the knowledge to address safety sensitivity specifically. Delving deeper into safety-related parameters during battery aging will facilitate the development of targeted safety assessment methodologies, further enhancing battery safety.

Author Contributions: Conceptualization, E.M., P.H., and J.M.; methodology, E.M., P.H., and J.M.; software, E.M.; validation, E.M.; formal analysis, E.M.; investigation, E.M.; resources, E.M.; data curation, E.M.; writing—original draft preparation, E.M.; writing—review and editing, E.M., P.H., S.M.A., C.E. and J.M.; visualization, E.M.; supervision, J.M.; project administration, C.E. and J.M.; funding acquisition, C.E. and J.M.. All authors have read and agreed to the published version of the manuscript.

Funding: This work originates from the research project SafeLIB. The COMET Project SafeLIB is funded within the framework of COMET—Competence Centers for Excellent Technologies (Grant agreement No. 882506) by BMK, BMDW, the Province of Upper Austria, the province of Styria as well as SFG. The COMET Program is managed by FFG. The authors thank the consortium members of the SafeLIB project for supporting this work. Supported by the Open Access Funding by the Graz University of Technology.

Data Availability Statement: Not applicable.

Acknowledgments: Open Access Funding by the Graz University of Technology. The authors thank the consortium members of the SafeLIB project for their valuable input to this work.

Conflicts of Interest: The authors declare no conflict of interest.

References

1. Garcia-Valle, R.; Peças Lopes, J.A. *Electric vehicle integration into modern power networks*; Springer: New York, London, 2013, ISBN 978-1-4614-0134-6.
2. Olsson, L.; Fallahi, S.; Schnurr, M.; Diener, D.; van Loon, P. Circular Business Models for Extended EV Battery Life. *Batteries* **2018**, *4*, 57, doi:10.3390/batteries4040057.
3. Hunt, G. US ABC Electric Vehicle Battery Test Procedures Manual, Revision 2. *principal author: Gary Hunt, Idaho National Engineering Laboratory (INEL), US Department of Energy Idaho Field Office, DOE/ID-10479, Rev 1996, 2, 39.*
4. Michelini, E.; Höschele, P.; Ratz, F.; Stadlbauer, M.; Rom, W.; Ellersdorfer, C.; Moser, J. Potential and Most Promising Second-Life Applications for Automotive Lithium-Ion Batteries Considering Technical, Economic and Legal Aspects. *Energies* **2023**, *16*, 2830, doi:10.3390/en16062830.
5. Han, X.; Ouyang, M.; Lu, L.; Li, J.; Zheng, Y.; Li, Z. A comparative study of commercial lithium ion battery cycle life in electrical vehicle: Aging mechanism identification. *Journal of Power Sources* **2014**, *251*, 38–54, doi:10.1016/j.jpowsour.2013.11.029.
6. Dubarry, M.; Truchot, C.; Liaw, B.Y. Synthesize battery degradation modes via a diagnostic and prognostic model. *Journal of Power Sources* **2012**, *219*, 204–216, doi:10.1016/j.jpowsour.2012.07.016.
7. Vetter, J.; Novák, P.; Wagner, M.R.; Veit, C.; Möller, K.-C.; Besenhard, J.O.; Winter, M.; Wohlfahrt-Mehrens, M.; Vogler, C.; Hammouche, A. Ageing mechanisms in lithium-ion batteries. *Journal of Power Sources* **2005**, *147*, 269–281, doi:10.1016/j.jpowsour.2005.01.006.
8. Birkel, C.R.; Roberts, M.R.; McTurk, E.; Bruce, P.G.; Howey, D.A. Degradation diagnostics for lithium ion cells. *Journal of Power Sources* **2017**, *341*, 373–386, doi:10.1016/j.jpowsour.2016.12.011.
9. Xiong, R.; Pan, Y.; Shen, W.; Li, H.; Sun, F. Lithium-ion battery aging mechanisms and diagnosis method for automotive applications: Recent advances and perspectives. *Renewable and Sustainable Energy Reviews* **2020**, *131*, 110048, doi:10.1016/j.rser.2020.110048.
10. Abada, S.; Petit, M.; Lecocq, A.; Marlair, G.; Sauvart-Moynot, V.; Huet, F. Combined experimental and modeling approaches of the thermal runaway of fresh and aged lithium-ion batteries. *Journal of Power Sources* **2018**, *399*, 264–273, doi:10.1016/j.jpowsour.2018.07.094.
11. Xie, S.; Ren, L.; Yang, X.; Wang, H.; Sun, Q.; Chen, X.; He, Y. Influence of cycling aging and ambient pressure on the thermal safety features of lithium-ion battery. *Journal of Power Sources* **2020**, *448*, 227425, doi:10.1016/j.jpowsour.2019.227425.
12. Preger, Y.; Torres-Castro, L.; Rauhala, T.; Jeevarajan, J. Perspective—On the Safety of Aged Lithium-Ion Batteries. *J. Electrochem. Soc.* **2022**, *169*, 30507, doi:10.1149/1945-7111/ac53cc.
13. Schmidt, A.; Smith, A.; Ehrenberg, H. Power capability and cyclic aging of commercial, high power lithium ion battery cells with respect to different cell designs. *Journal of Power Sources* **2019**, *425*, 27–38, doi:10.1016/j.jpowsour.2019.03.075.
14. Han, X.; Lu, L.; Zheng, Y.; Feng, X.; Li, Z.; Li, J.; Ouyang, M. A review on the key issues of the lithium ion battery degradation among the whole life cycle. *eTransportation* **2019**, *1*, 100005, doi:10.1016/j.etrans.2019.100005.
15. Rufino Júnior, C.A.; Sanseverino, E.R.; Gallo, P.; Koch, D.; Kotak, Y.; Schweiger, H.-G.; Zanin, H. Reviewing Regulations and Standards for Second-Life Batteries **2023**, doi:10.20944/preprints202306.0711.v1.
16. Zhou, W.; Lu, Q.; Zheng, Y. Review on the Selection of Health Indicator for Lithium Ion Batteries. *Machines* **2022**, *10*, 512, doi:10.3390/machines10070512.
17. Dubarry, M.; Truchot, C.; Liaw, B.Y. Synthesize battery degradation modes via a diagnostic and prognostic model. *Journal of Power Sources* **2012**, *219*, 204–216, doi:10.1016/j.jpowsour.2012.07.016.

18. Xiong, W.; Xu, G.; Li, Y.; Zhang, F.; Ye, P.; Li, B. Early prediction of lithium-ion battery cycle life based on voltage-capacity discharge curves. *Journal of Energy Storage* **2023**, *62*, 106790, doi:10.1016/j.est.2023.106790. 567 568
19. Anseán, D.; Dubarry, M.; Devie, A.; Liaw, B.Y.; García, V.M.; Viera, J.C.; González, M. Fast charging technique for high power LiFePO₄ batteries: A mechanistic analysis of aging. *Journal of Power Sources* **2016**, *321*, 201–209, doi:10.1016/j.jpowsour.2016.04.140. 569 570 571
20. Wei, M.; Gu, H.; Ye, M.; Wang, Q.; Xu, X.; Wu, C. Remaining useful life prediction of lithium-ion batteries based on Monte Carlo Dropout and gated recurrent unit. *Energy Reports* **2021**, *7*, 2862–2871, doi:10.1016/j.egyr.2021.05.019. 572 573 574
21. Sun, Y.; Hao, X.; Pecht, M.; Zhou, Y. Remaining useful life prediction for lithium-ion batteries based on an integrated health indicator. *Microelectronics Reliability* **2018**, *88–90*, 1189–1194, doi:10.1016/j.microrel.2018.07.047. 575 576
22. Eddahech, A.; Briat, O.; Vinassa, J.-M. Determination of lithium-ion battery state-of-health based on constant-voltage charge phase. *Journal of Power Sources* **2014**, *258*, 218–227, doi:10.1016/j.jpowsour.2014.02.020. 577 578
23. Yang, F.; Wang, D.; Zhao, Y.; Tsui, K.-L.; Bae, S.J. A study of the relationship between coulombic efficiency and capacity degradation of commercial lithium-ion batteries. *Energy* **2018**, *145*, 486–495, doi:10.1016/j.energy.2017.12.144. 579 580 581
24. Wang, R.; Feng, H. Remaining useful life prediction of lithium-ion battery using a novel health indicator. *Qual. Reliab. Engng. Int.* **2021**, *37*, 1232–1243, doi:10.1002/qre.2792. 582 583
25. Tseng, K.-H.; Liang, J.-W.; Chang, W.; Huang, S.-C. Regression Models Using Fully Discharged Voltage and Internal Resistance for State of Health Estimation of Lithium-Ion Batteries. *Energies* **2015**, *8*, 2889–2907, doi:10.3390/en8042889. 584 585 586
26. Baghdadi, I.; Briat, O.; Gyan, P.; Vinassa, J.M. State of health assessment for lithium batteries based on voltage–time relaxation measure. *Electrochimica Acta* **2016**, *194*, 461–472, doi:10.1016/j.electacta.2016.02.109. 587 588
27. Schmidt, J.P.; Tran, H.Y.; Richter, J.; Ivers-Tiffée, E.; Wohlfahrt-Mehrens, M. Analysis and prediction of the open circuit potential of lithium-ion cells. *Journal of Power Sources* **2013**, *239*, 696–704, doi:10.1016/j.jpowsour.2012.11.101. 589 590 591
28. Menale, C.; D'Annibale, F.; Mazzarotta, B.; Bubbico, R. Thermal management of lithium-ion batteries: An experimental investigation. *Energy* **2019**, *182*, 57–71, doi:10.1016/j.energy.2019.06.017. 592 593
29. Waldmann, T.; Wilka, M.; Kasper, M.; Fleischhammer, M.; Wohlfahrt-Mehrens, M. Temperature dependent ageing mechanisms in Lithium-ion batteries – A Post-Mortem study. *Journal of Power Sources* **2014**, *262*, 129–135, doi:10.1016/j.jpowsour.2014.03.112. 594 595 596
30. Xiong, R.; He, H.; Sun, F.; Zhao, K. Evaluation on State of Charge Estimation of Batteries With Adaptive Extended Kalman Filter by Experiment Approach. *IEEE Trans. Veh. Technol.* **2013**, *62*, 108–117, doi:10.1109/TVT.2012.2222684. 597 598 599
31. Zhang, S.S. A review on the separators of liquid electrolyte Li-ion batteries. *Journal of Power Sources* **2007**, *164*, 351–364, doi:10.1016/j.jpowsour.2006.10.065. 600 601
32. Ng, K.S.; Moo, C.-S.; Chen, Y.-P.; Hsieh, Y.-C. Enhanced coulomb counting method for estimating state-of-charge and state-of-health of lithium-ion batteries. *Applied Energy* **2009**, *86*, 1506–1511, doi:10.1016/j.apenergy.2008.11.021. 602 603 604
33. Tong, S.; Klein, M.P.; Park, J.W. On-line optimization of battery open circuit voltage for improved state-of-charge and state-of-health estimation. *Journal of Power Sources* **2015**, *293*, 416–428, doi:10.1016/j.jpowsour.2015.03.157. 605 606

34. Weng, C.; Sun, J.; Peng, H. A unified open-circuit-voltage model of lithium-ion batteries for state-of-charge estimation and state-of-health monitoring. *Journal of Power Sources* **2014**, *258*, 228–237, doi:10.1016/j.jpowsour.2014.02.026. 607–609
35. Xing, Y.; He, W.; Pecht, M.; Tsui, K.L. State of charge estimation of lithium-ion batteries using the open-circuit voltage at various ambient temperatures. *Applied Energy* **2014**, *113*, 106–115, doi:10.1016/j.apenergy.2013.07.008. 610–611
36. Plett, G.L. Extended Kalman filtering for battery management systems of LiPB-based HEV battery packs. *Journal of Power Sources* **2004**, *134*, 277–292, doi:10.1016/j.jpowsour.2004.02.033. 612–613
37. Dreyer, W.; Jamnik, J.; Gohlke, C.; Huth, R.; Moskon, J.; Gaberscek, M. The thermodynamic origin of hysteresis in insertion batteries. *Nat. Mater.* **2010**, *9*, 448–453, doi:10.1038/nmat2730. 614–615
38. Chen, X.; Hu, Y.; Li, S.; Wang, Y.; Li, D.; Luo, C.; Xue, X.; Xu, F.; Zhang, Z.; Gong, Z.; et al. State of health (SoH) estimation and degradation modes analysis of pouch NMC532/graphite Li-ion battery. *Journal of Power Sources* **2021**, *498*, 229884, doi:10.1016/j.jpowsour.2021.229884. 616–618
39. Li, J.; Adewuyi, K.; Lotfi, N.; Landers, R.G.; Park, J. A single particle model with chemical/mechanical degradation physics for lithium ion battery State of Health (SOH) estimation. *Applied Energy* **2018**, *212*, 1178–1190, doi:10.1016/j.apenergy.2018.01.011. 619–621
40. Gyenes, B.; Stevens, D.A.; Chevrier, V.L.; Dahn, J.R. Understanding Anomalous Behavior in Coulombic Efficiency Measurements on Li-Ion Batteries. *J. Electrochem. Soc.* **2014**, *162*, A278–A283, doi:10.1149/2.0191503jes. 622–623
41. Deshpande, R.D.; Ridgway, P.; Fu, Y.; Zhang, W.; Cai, J.; Battaglia, V. The Limited Effect of VC in Graphite/NMC Cells. *J. Electrochem. Soc.* **2014**, *162*, A330–A338, doi:10.1149/2.0221503jes. 624–625
42. Xu, J.; Deshpande, R.D.; Pan, J.; Cheng, Y.-T.; Battaglia, V.S. Electrode Side Reactions, Capacity Loss and Mechanical Degradation in Lithium-Ion Batteries. *J. Electrochem. Soc.* **2015**, *162*, A2026–A2035, doi:10.1149/2.0291510jes. 626–628
43. Diao, W.; Saxena, S.; Han, B.; Pecht, M. Algorithm to Determine the Knee Point on Capacity Fade Curves of Lithium-Ion Cells. *Energies* **2019**, *12*, 2910, doi:10.3390/en12152910. 629–630
44. Saha, B.; Goebel, K. Modeling Li-ion Battery Capacity Depletion in a Particle Filtering Framework. *Annual Conference of the PHM Society* **2021**. 631–632
45. Williard, N.; He, W.; Osterman, M.; Pecht, M. Comparative Analysis of Features for Determining State of Health in Lithium-Ion Batteries. *IJPHM* **2013**, *4*, doi:10.36001/ijphm.2013.v4i1.1437. 633–634
46. Yun, Z.; Qin, W. Remaining Useful Life Estimation of Lithium-Ion Batteries Based on Optimal Time Series Health Indicator. *IEEE Access* **2020**, *8*, 55447–55461, doi:10.1109/ACCESS.2020.2981947. 635–636
47. Ruan, H.; He, H.; Wei, Z.; Quan, Z.; Li, Y. State of Health Estimation of Lithium-ion Battery Based on Constant-Voltage Charging Reconstruction. *IEEE J. Emerg. Sel. Topics Power Electron.* **2021**, *1*, doi:10.1109/JESTPE.2021.3098836. 637–639
48. Tarascon, J.M.; Armand, M. Issues and challenges facing rechargeable lithium batteries. *Nature* **2001**, *414*, 359–367, doi:10.1038/35104644. 640–641
49. Bodenes, L.; Naturel, R.; Martinez, H.; Dedryvère, R.; Menetrier, M.; Croguennec, L.; Pérès, J.-P.; Tessier, C.; Fischer, F. Lithium secondary batteries working at very high temperature: Capacity fade and understanding of aging mechanisms. *Journal of Power Sources* **2013**, *236*, 265–275, doi:10.1016/j.jpowsour.2013.02.067. 642–644
50. Stiaszny, B.; Ziegler, J.C.; Krauß, E.E.; Schmidt, J.P.; Ivers-Tiffée, E. Electrochemical characterization and post-mortem analysis of aged LiMn2O4–Li(Ni0.5Mn0.3Co0.2)O2/graphite lithium ion batteries. Part I: Cycle aging. *Journal of Power Sources* **2014**, *251*, 439–450, doi:10.1016/j.jpowsour.2013.11.080. 645–647

-
51. Michelini, E.; Höschele, P.; Heindl, S.F.; Erker, S.; Ellersdorfer, C. Experimental Investigation on Reversible Swelling Mechanisms of Lithium-Ion Batteries under a Varying Preload Force. *Batteries* **2023**, *9*, 218, doi:10.3390/batteries9040218. 648
649
650
52. Choudhari, V.G.; Dhoble, A.S.; Sathe, T.M. A review on effect of heat generation and various thermal management systems for lithium ion battery used for electric vehicle. *Journal of Energy Storage* **2020**, *32*, 101729, doi:10.1016/j.est.2020.101729. 651
652
653
53. Xie, Y.; Wang, S.; Li, R.; Ren, D.; Yi, M.; Xu, C.; Han, X.; Lu, L.; Friess, B.; Offer, G.; et al. Inhomogeneous degradation induced by lithium plating in a large-format lithium-ion battery. *Journal of Power Sources* **2022**, *542*, 231753, doi:10.1016/j.jpowsour.2022.231753. 654
655
656
657